Confined buckling in thin sheets and its correlation to ripplocations: A deformation mechanism in layered solids

H. O. Badr,[1] X. Zhao,[2] S. Koumlis,[2] G. J. Tucker,[2] L. Lamberson,[2,*] and M. W. Barsoum[1,†]
[1]*Department of Materials Science and Engineering, Drexel University, Philadelphia, Pennsylvania 19104, USA*
[2]*Department of Mechanical Engineering, Colorado School of Mines, Golden, Colorado, 80401, USA*

(Received 31 May 2020; accepted 23 July 2021; published 7 September 2021)

Recently, we have established that, when loaded in compression, edge-on, atomic layers in layered solid can fail by buckling. The resulting structure is termed a ripplocation. When more than one layer buckles, they outline standing waves with boundaries that we labeled ripplocation boundaries that are nearly fully recoverable. In this paper, we examine buckling of layers at the centimeter level to explore continuum buckling theory and its applicability to atomic layers. Specifically, we examine buckling by confining and cyclically loading thin steel sheets, edge-on, determining that increasing confining pressure, sheet thickness, and/or decreasing the number of layers increases the buckling load. Concomitantly, the resulting wavelengths and amplitudes are reduced. A nonlinear, folding mechanics model, which accounts for frictional bending and foundation energies, is adapted and verified on our experimental results. We also demonstrate that Coulombic friction between the layers can account for the energy dissipated per cycle. The predicted values of buckling nucleation loads and number of modes from the model are in good agreement—at low levels of confinement—with continuum and atomistic scale results. The wavelength estimates from the model correlate surprisingly well with the continuum buckling results; however, likely due to the complex mechanics at the lower length scales and limiting theoretical assumptions in the derivation, the accuracy decreases at the atomistic scale and at higher confining pressures.

DOI: 10.1103/PhysRevMaterials.5.093603

I. INTRODUCTION

Buckling, on the one hand, and layered materials, solids, and formations, on the other, have been most intimately intertwined since humanity started thinking about how they deformed. It has long been appreciated that, under the right conditions, compressively loading a layered system—be they layered solids [1–4], geologic formations [5–7], or laminated composites [8–10], card decks [11], etc.—edge-on will result, more often than not, in a buckling of the layers that, in turn, leads to kink band (KB) formation.

At the macroscale, the commonalities between layered materials and geologic formations have been long appreciated and well covered in a recent theme issue [4]. The question of folding of parallel layers has also been one of study in layered crystalline solids (LCSs); after all, LCSs such as graphite, the MAX phases, mica, and other layered silicates also unambiguously fail by the formation of KBs when the layers are compressively loaded edge-on. Crucially, the commonalities across the micro- to macrolength scales have never been addressed. This disconnect came about because it has long been assumed that LCSs deformed via the nucleation and propagation of basal dislocations (BDs) [12] that are senseless in the macroworld.

Recently, we showed that, in layered systems in general and LCSs in particular, between linear elasticity and KB formation, there is an important kinking nonlinear elastic (KNE) regime where ripplocations (see below) play an important role [11,13–18]. Ripplocations, at least in graphite, are highly mobile, fully recoverable, dissipative waves that form—down to the single atomic layer scale—because of confined buckling. If one layer buckles, it is termed a ripplocation. When multiple layers buckle, they form standing waves, the crests and troughs of which define ripplocation boundaries (RBs) [11,14]. In contrast to KBs that are irreversible, RBs are fully reversible/recoverable. Moreover, the friction associated with the to-and-fro motion of the ripplocations was assumed to account for the energy dissipated observed when layered solids are cyclically loaded [11,15]. In our previous work, we assumed that BD-based incipient KBs were responsible for this energy dissipation [12,19], which in retrospect is at the very least incomplete and, more likely than not, incorrect.

The term *ripplocations* was coined by Kushima *et al.* [20] to describe surface/near-surface defects in van der Waals solids. They elegantly showed via a combination of density functional theory (DFT) and molecular dynamics (MD) modeling that ripplocations were different than BDs because two ripplocations of the same sign attracted [20]. They also imaged with a high-resolution transmission electron microscope (HRTEM) near-surface ripplocations in MoS_2 [20].

We used a combination of MD modeling on graphite at 10 K and nanoindentation (NI) experiments on Ti_3SiC_2—a layered, machinable ceramic—to show that ripplocations are probably the operative deformation mechanism in most LCSs and that, at least in graphite, they have no polarities [15,16].

*Corresponding author: barsoumw@drexel.edu
†Corresponding author: les@mines.edu

In the same work, we provided indirect TEM evidence for ripplocations. Aslin *et al.* [17] provided direct HRTEM evidence for microscopic features that were incompatible with BDs but in line with ripplocations in naturally deformed biotite. In previous work, we confined and aluminum thin sheets and cyclically indented them with a cylindrical indenter and presented evidence of buckling that scaled with bulk RBs [11]. We carried out the same experiment *in silico* on graphite at 10 K and showed that the exact same response occurred at the atomic level and that ripplocations appear to be a widespread mechanism for the deformation of LCSs. März *et al.* [21] conducted similar experiments by indenting graphite single crystal *in silico* using a sharp quadratic indenter and by introducing voids/defects to the simulation cell. Following these conditions, they presented an elucidating image for the initiation and evolution of KBs in graphite. Moreover, they provided experimental evidence for basal plane bending/RBs in graphite using HRTEM [21,22]. Alaferdov *et al.* [23] presented further TEM evidence for ripplocations that formed in graphite nanoplatelets because of sonication-assisted liquid phase exfoliation.

The mechanics of buckling instabilities leading to KB formation of layered structures at the continuum scale has received considerably more attention, particularly in the areas of classical laminate composite theory and geological formations. Regular period waveforms have been habitually documented in layered geological outcrops [24–26]. Their formation has been considered theoretically from an elastic perspective (e.g., Currie *et al.* [27] and Johnson and Honea [28], among others), as well as in the laboratory-scale experiments (Kuenen and de Sitter [29] and Blay *et al.* [30], among others). However, many of these studies concentrated on perfectly adhered (ignoring the layers) or freely sliding layer assumptions. Budd *et al.* [31], with the consideration of overburden (confinement) pressure, developed a formulation of a frictional model for folding. The buckling model presented here stems from the efforts of Budd *et al.* [31], in addition to work by Wadee *et al.* [1], the multilayer folding models of Wadee and Edmunds [2], and Wadee [32].

In the composite community, the mechanics of buckling growth and development was well studied by Chai [33], Katz and Givli [34], Roman and Pocheau [35], and others [36,37] using polycarbonate and steel single beams/plates. This paper was developed to understand the buckling-induced subsurface delaminations in laminated composites. In the same respect, seminal efforts by Budiansky and Fleck [38], among others, examined KB propagation in layered fiber composites both experimentally and analytically. In polymer matrix composites, evidence was presented to suggest that the kinking compressive strength is governed by fiber misalignment (i.e., an initiating defect). There are numerous general reviews of the kinking phenomena in composites [38–41]. Additionally, complementary finite element analysis has also been extensively used to study the initiation and evolution of KBs in composites [42–46]. While on a different material system and length scale, these studies provide useful insight on KB formation, with relevant commonalities to our investigation.

In this paper, we investigate the fundamental mechanics of buckling instabilities of a layered system. In doing so, we explored the effects of confinement, friction, and geometry on salient buckling features at the continuum level. To this end, we cyclically loaded, edge-on, decks of thin steel sheets and measured the critical stress at which buckling nucleated σ_{RB}, which herein we take as the nucleation stress of the RBs, for the sake of comparing our result with atomistic-level buckling phenomena we observed previously. We also measured the wavelengths λ_{RB} and amplitudes A_{RB} of these RBs and the energy dissipated per unit volume per cycle W_d as a function of (i) number of sheets per deck (spd), (ii) individual sheet thicknesses, t, and (iii) initial confining pressure $P_{N,0}$. It should be noted that, in the geological literature, $P_{N,0}$ is referred to as an overburden pressure. Our results clearly show that increasing the effective $P_{N,0}$ increases σ_{RB} and W_d but decreases λ_{RB} and A_{RB}.

We further adopted, developed, and verified a mechanics model that was found to be robust in capturing the physics of the deformation of layered solids at the macroscale but, most importantly, also at the atomic layer scale. In that, the features of RBs, nucleation load, and wavelength were well predicted at both the continuum and the atomistic scale. We also demonstrate that Coulombic friction between the layers can account for W_d.

II. EXPERIMENTAL DETAILS

The experimental configuration, imaging, and measurement systems used are described in detail in an earlier work [11]. In brief, various decks of thin steel sheets were placed between a fixed and a translating block, as shown schematically in Fig. 1(a). The height H of the deck was 40 ± 0.1 mm, and the number of layers per deck varied. Once set, an initial lateral overburden pressure was applied. A subset of the layers was then loaded, edge-on, with a 2.34 mm-diameter cylindrical indenter, with its axis parallel to the indented layers [Fig. 1(a)]. All experiments were carried out using a Shimadzu AG-IS Load Frame equipped with a 50 kN load cell, and an Epsilon LVDT deflectometer. *In situ* images were recorded at a frame rate of 5 fps using a Stingray F-504 camera (2452×2056 pixels) with a Nikon 105 mm lens and 8W LED lights. In a typical experiment, the indenter is thrust into the layers—in a displacement-controlled mode—to a maximum indentation depth of 2.5 mm $h_{2.5}$ [point Y in Fig. 1(b)], retracted to a $h < h_{2.5}$ [point X in Fig. 1(b)], reloaded to $h_{2.5}$, and unloaded to progressively lower h values. This protocol results in nearly fully recoverable nested loops, as shown schematically in Fig. 1(b).

In addition to recording the indentation loads and displacements, we also measured the confining pressure P_N using a load cell attached to the translating block holding the layers with initial confining pressure $P_{N,0}$ [Fig. 1(a)]. The confining pressure was displacement controlled so that it could evolve with the indentation load [Figs. 1(c) and 1(d)].

The coordinate system used is shown in Fig. 1(a). Most of the work was carried out with steel sheets with thicknesses t of 0.127 mm. To explore the effect of sheet thickness, in two runs, t was 0.0508 mm. In the remainder of this paper, these values will be rounded off to 0.13 and 0.05 mm, respectively. A spring steel (1095 spring steel, MacMaster Carr, New Jer-

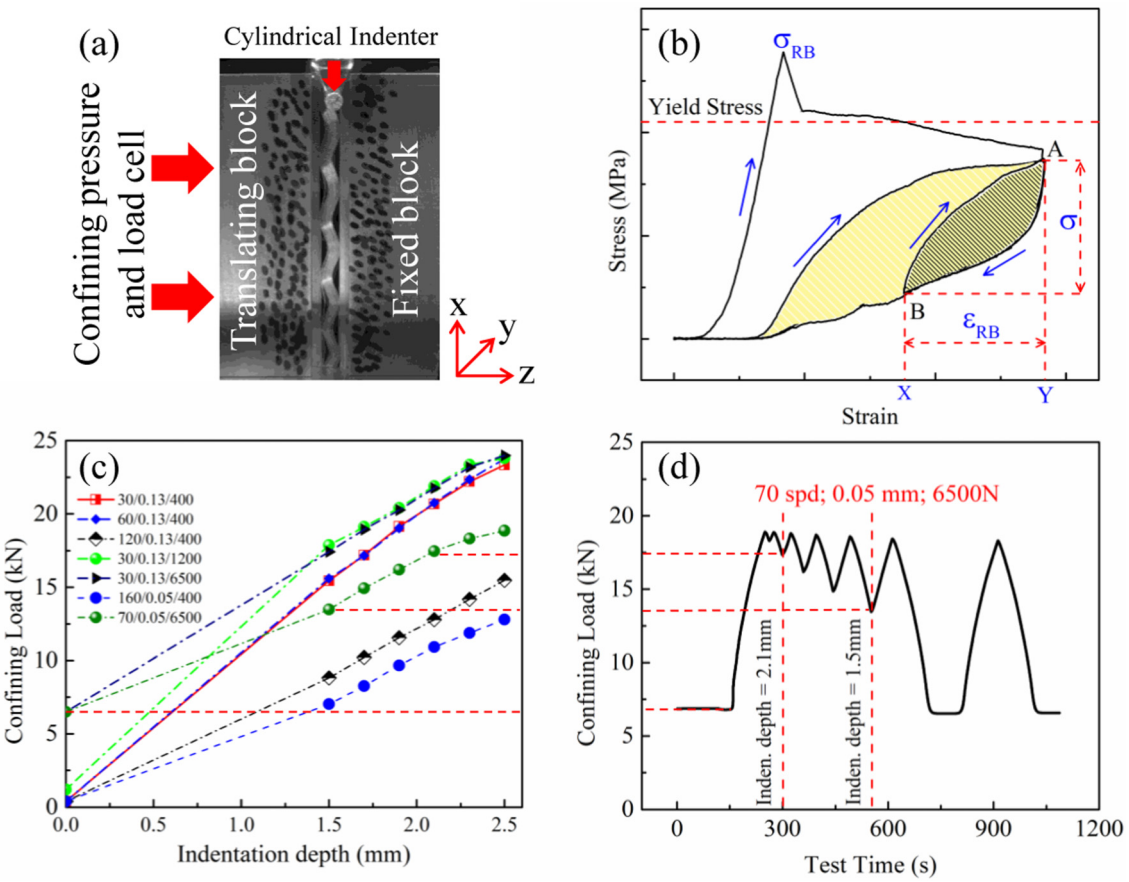

FIG. 1. (a) Experimental setup and coordinate system used. (b) Schematic showing typical loading/unloading protocol. In all cases, a cylindrical indenter was indented to a displacement corresponding to the maximum strain Y, unloaded to strain X, and reloaded to Y to yield a fully recoverable loop designated by hatched area. The process was then repeated for increasing values of unloading strains, resulting in fully recoverable nested loops sharing a single unloading trajectory (see Fig. 4). Before dismantling the setup, one last cycle (colored yellow) was carried out. (c) Plot of constraining loads as a function of indentation depth. (d) Actual constraining load as a function of time during cycling. Horizontal dashed red lines connect (c) and (d).

sey) was used for all seven experiments carried out. As noted above, all experiments were imaged.

To convert the indentation loads to stresses, the indenter was assumed to be flat with an area A_{ind} given by the product of $n \times t \times b$, where n is number of buckled layers (counted from image still frames at the point of maximum indentation depth), and b is their width (30 ± 0.2 mm). This value of n was double checked macroscopically by counting the number of plastically deformed layers after complete load unloading and removal of the layers from the frame (see below). To calculate the strain due to the RBs, ε_{RB}, the recorded indentation depths in millimeters were divided by the initial deck height, viz. 40 ± 0.1 mm.

The load at which the RBs were first observed was determined from the camera images. This load was then converted to a σ_{RB} [Fig. 1(b)] in the same way as described above. The values of λ_{RB} and radius of curvature R were measured from still frames at the onset of buckling (Figs. S1(a)–S1(g) in the Supplemental Material [47]) using the image analysis software IMAGEJ [48], while the values of A_{RB} and number of modes g were obtained following the same measurement protocol but at the point of maximum indentation depth (Figs. S1(a″)–S1(g″) in the Supplemental Material [47]). Note that g (i.e., where the curvature of the ripple changes sign) did not change with indentation, and the point of maximum depth was chosen as a clear point for accurate counting.

As in our previous work, W_d was calculated from the area enclosed by each nested loop. Referring to Fig. 1(b), the area of the first unloading loop is given by the hatched area, and the nonlinear strain associated with this cycle is simply the difference between X and Y. The maximum stress associated with this loop is the difference between the stresses at A and B in Fig. 1(b). Said otherwise, as in our previous work, the origin is shifted to Point A.

III. THEORETICAL CONSIDERATIONS OF MULTILAYER BUCKLING

The model used for our continuum investigation is based on the original models of nonlinear folds by Budd *et al.* [31] and Edmunds *et al.* [3] These models use an energetic approach, where the nonlinear effect of friction is considered, and the critical load at buckling (i.e., fold formation) and resulting λ_{RB} are predicted from a Galerkin approximation substituted into a linearized potential energy function. Specifically, this approach uses a linearized differential equa-

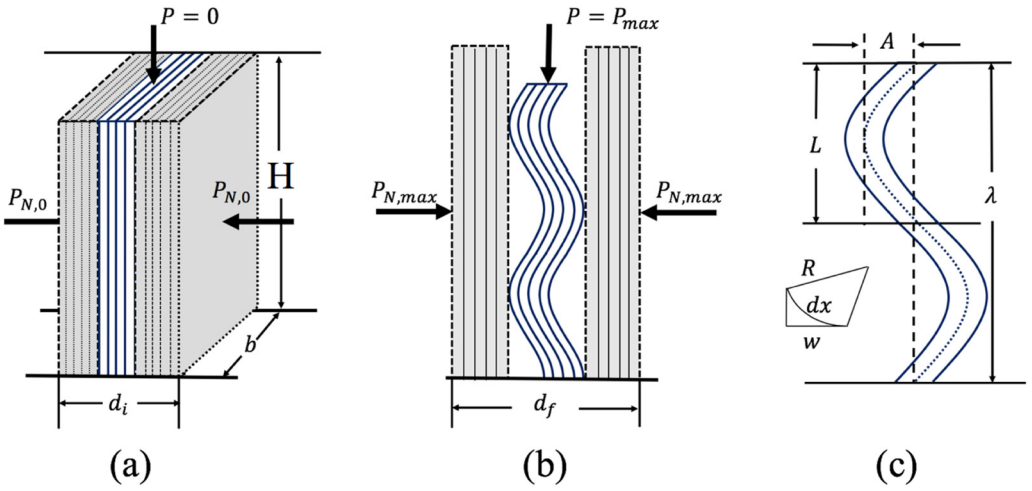

FIG. 2. (a) Initial configuration where layers are confined by force $P_{N,0}$, (b) Configuration at maximum indentation $h_{2.5}$, showing vertically loaded four layers that buckled into four modes. (c) Definitions of w, wavelength $\lambda = 2L$, and amplitude A_{RB}.

tion under nonlinear boundary conditions that capture most of the significant buckling mechanisms (vs. a full nonlinear formulation). Budd *et al.* [31] described parallel folding behavior of two layers under compression that are allowed to slip relative to one another, as well as folding along a center line of finite curvature due to overburden pressure (here, we term this confinement). Edmunds *et al.* [3] tackled multilayer structures that are more relevant to our experiments. However, both investigations considered the buckling layers to be embedded in a soft foundation. Here, we differ, as the compressed layers are held in stiff confinement, and thus, we use a slightly different means to extract our transverse stiffness parameter (see below). We proceed through the details of the model used in this investigation, schematically shown in Figs. 2(a)–2(c), as follows.

Consider n incompressible layers of thickness t and width b [Fig. 2(a)], and the total thickness of n buckled layers is $T = nt$ formed from a material with flexural rigidity EI. These layers are compressed axially by a load P [Fig. 2(b)], and the flexural rigidity of each layer is given by

$$EI = \frac{Ebt^3}{12}, \tag{1}$$

where E is Young's modulus of the material comprising the layers (herein referred to as sheets). We assume that all the buckled layers bend about the same central line of the curvature, and slip is constant between layers and no voids develop.

The confining force P_N is applied along the height H of layers with an initial confinement $P_{N,0}$ [Fig. 2(a)]. The remaining unbuckled layers, together with the rigid fixture on each side, act as the foundation and are modeled by two springs in series, each with a spring constant k per unit length. Experimentally, plots of the confinement force vs displacement [Fig. 1(c)] were nominally straight, indicating linear stiffnesses. For all experiments, the transverse stiffness of the foundation c is determined assuming

$$c = \frac{\Delta P_N}{\Delta d} = \frac{P_{N,\max} - P_{N,0}}{A_{RB}}, \qquad k = \frac{2c}{H}, \tag{2}$$

where $P_{N,\max}$ is the confinement load at maximum indentation. The horizontal deflection of the spring Δd is the difference between the initial and final (viz. at maximum load) amplitude of buckling [see Figs. 2(a) and 2(b)], which we equate to A_{RB}. The measured unit stiffness results from two springs in series, and as such, k is twice c divided by H. This manipulation is performed to obtain a stiffness per unit length.

Assuming small deformations, with a coordinate of arclength x and relatively small deflection w [Fig. 2(c)], the nonlinearity of the geometry is not considered dominant and is neglected. The total potential energy function V for this case includes the bending energy U_B, the work done by the vertical load U_P, the foundation energy U_F, and the work done by friction U_μ. Working under the assumption of $T^2 \ll 4n^2R^2/(n-1)^2$ (i.e., that the radius of curvature R over the number of buckled layers during buckling is greater than $T = nt$), V over a periodic half-wavelength L can be written as the balance of

$$V = U_B - U_p + U_F + U_\mu,$$

where, as shown by Edmunds *et al.* [3] is

$$V = \int_0^L \left[\frac{nEI}{2}\ddot{w}^2 - \frac{P}{2}\dot{w}^2 + \frac{k}{2}w^2 + \frac{(n-1)\chi\mu qT|\dot{w}|}{n}\right]dx. \tag{3}$$

For this paper, μ is the friction coefficient that we obtained experimentally using the inclined plane method [11]. The μ values measured for the thick and thin steel sheets used herein are 0.23 and 0.27, respectively. Moreover, χ is a friction indicator, where $\chi = +1$ designates that the direction of the friction force is opposite to the external load and hence resists the release of strain energy. Said otherwise, the friction energy contribution to V is positive. Conversely, when $\chi = -1$, a negative contribution to V is designated, where the direction of the friction force is the same as the loading direction.

Using a Galerkin approximation and assuming a deflection shape of $w(x) = A\cos(\pi x/L)$, where A is the amplitude of the wave, the linear eigenvalue analysis of V provides the critical

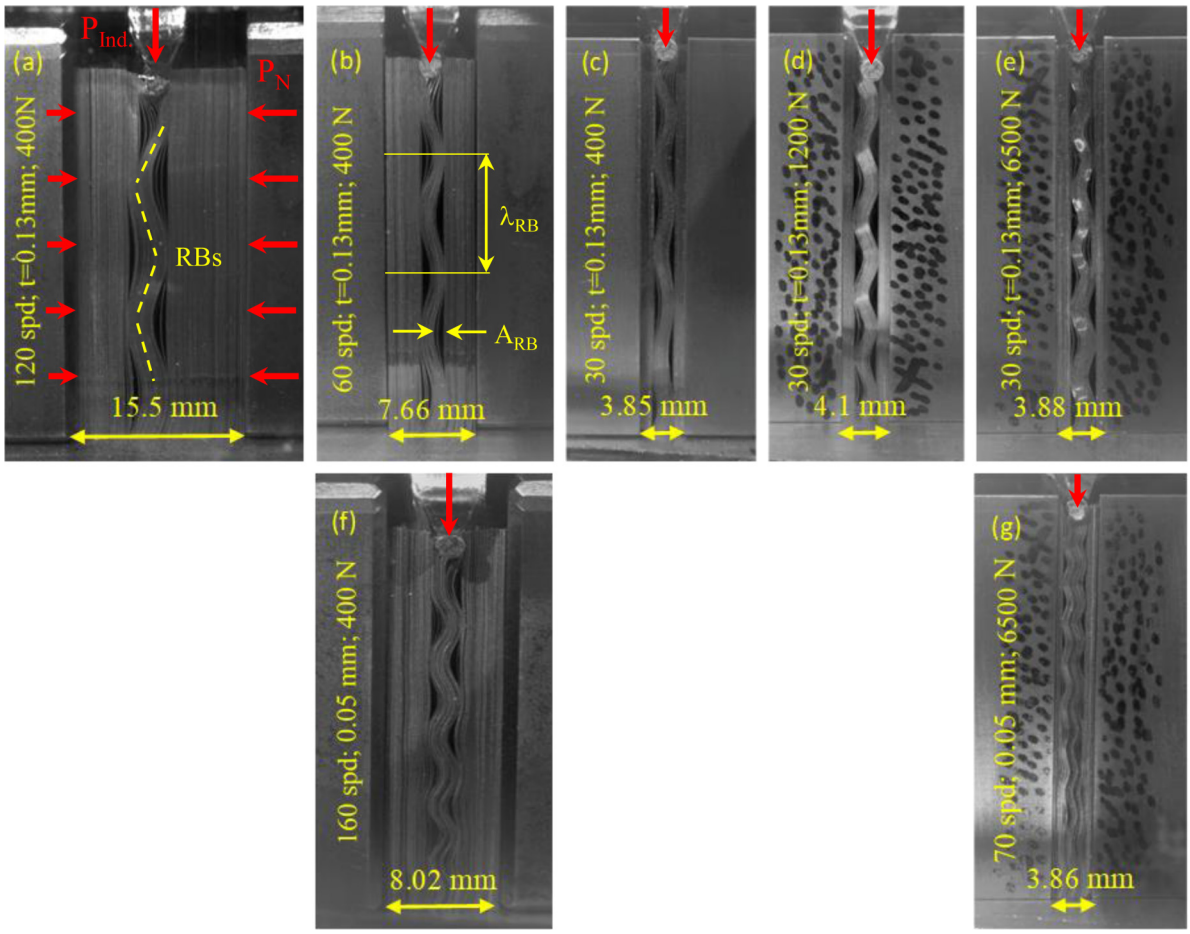

FIG. 3. Pictures of steel decks at maximum indentations for runs (a) 120-0.13-400, (b) 60-0.13-400, (c) 30-0.13-400, (d) 30-0.13-1200, (e) 30-0.13-6500, (f) 160-0.05-400, and (g) 70-0.05-6500. The vertically stacked panels differ in the thicknesses of sheets used (top = 0.13; bottom = 0.05). Horizontal red arrows denote lateral confining loads, while the vertical ones denote indentation direction.

load [3]:

$$P_{\text{crit}} = \frac{n\pi^2 EI}{L^2} + \frac{kL^2}{\pi^2}. \tag{4}$$

Minimizing the critical load with respect to the half-wavelength yields

$$L = \pi\left(\frac{nEI}{k}\right)^{1/4} = \pi\left(\frac{nEbt^3}{12k}\right)^{1/4}. \tag{5}$$

The theoretical buckling modes g are obtained by assuming

$$g = \frac{2H}{\lambda} = \frac{H}{L}. \tag{6}$$

Interestingly, μ does not factor into any of these expressions, despite being explicitly considered in the model.

The theoretical P_{crit}, L, and g values determined from Eqs. (4) to (6), respectively, are then compared with experimentally measured ones. Empirically, g is determined by counting the number of inflection points (i.e., where the curvature of the ripple changes sign) in the still images.

Note that the assumption

$$T^2 \ll \frac{4n^2R^2}{(n-1)^2},$$

indicates that the difference among the bending energy in n layers are negligible, and the total bending energy can be represented as n times the bending energy measured from the middle of layers. When tested, this simplification worked well at low confinement levels with a rigid foundation, with only 2% error when compared with the sum of n terms. While at higher confinement levels, this simplification underestimates the total energy by values up to 30% because the curvatures decrease to on the order of, or less than, the overall thickness of the buckled layers. Attempting to get a measuring scale, we introduced the following term:

$$\eta = \frac{4n^2R^2}{(n-1)^2T^2},$$

which is essentially a nondimensionalized ratio of the curvature and overall thickness of the buckled layers as an indicator of how well the aforementioned inequality holds based on the model assumptions. The higher the η value, the higher the R values, and the better the model predictions and experiments align. In other words, agreement between theory and experiment is best at large η values and becomes increasingly less so at higher levels of confinement, i.e., for $\eta < 112$.

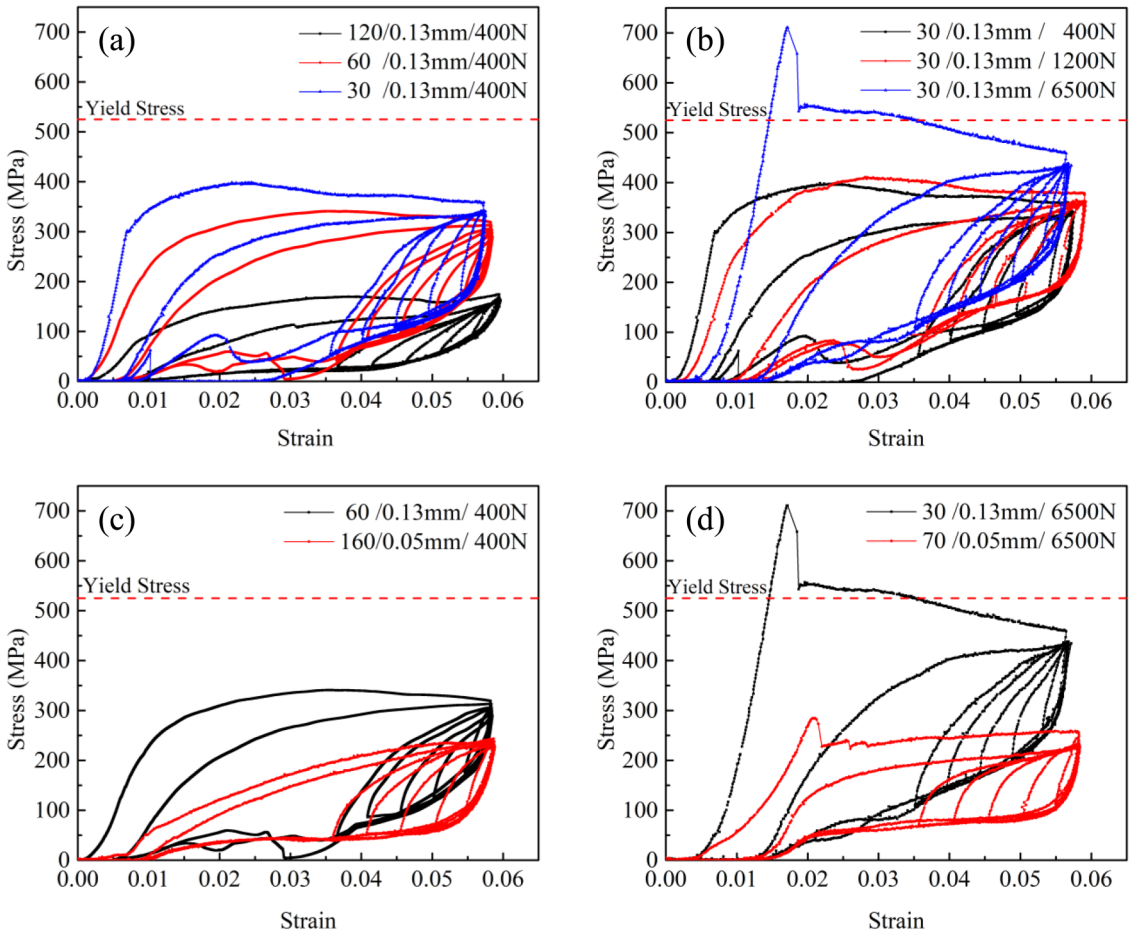

FIG. 4. Indentation stress-strain curves as a function of (a) number of sheets per deck at $P_{N,0}$ 400 N and $t = 0.13$ mm, (b) $P_{N,0}$ for a deck of 30 sheets, 0.13 mm thick, (c) t at $P_{N,0}$ of 400 N and 60 and 160 sheets for the thick and thin sheets, respectively, and (d) same as (c) but at a $P_{N,0}$ of 6500 N with 30 and 70 sheets for the thick and thin sheets, respectively. Note that, in all cases, after the nested loops were obtained, the indenter load was fully removed and then reapplied to obtain a second full cycle. The yield stress of the steel is shown in all plots as a horizontal dashed line.

IV. RESULTS

It is important at the outset to point out what the camera images of all experiments demonstrate: At a critical load, a confined, collective, rapid buckling of the layers directly under the indenter occurs. The deformation is delocalized and appears (at least with the framing rates used during experimentation) rather instantaneously, reaching the bottom platen forming a standing wave with a clear number of modes. With further penetration of the indenter, there is little change in λ_{RB}, but A_{RB} increases. Changes of λ_{RB} with indentation are discussed in detail in the Supplemental Material [47].

A total of seven indentation experiments were conducted under various confinement conditions. For brevity, these experiments will be henceforth referred to as: *xx-yy-zz*, where the first number denotes the spd, the second t in mm, and the third $P_{N,0}$ in N. The first three experiments compared three runs (i.e., 120-0.13-400, 60-0.13-400, and 30-0.13-400), where the only variable was the spd. The results in Figs. 3(a)–3(c), respectively, clearly show that by increasing, in this case, the "effective" constraining pressure by reducing spd, both λ_{RB} and A_{RB} decrease. This comes about because increasing the deck width introduces more microscopic air gaps between the sheets that effectively render the system more compliant in the z direction. This is best seen in Fig. 1(c), where P_N is plotted vs indentation depth. For the 120-sheet deck [black half-filled squares in Fig. 1(c)], P_N is significantly lower throughout the experiment than the other decks. Using the same logic, decreasing the initial deck width and/or increasing $P_{N,0}$ results in a significant decrease in the spread of P_N values, as shown in Fig. 1(c).

The second set (30-0.13-400, 30-0.13-1200, and 30-0.13-6500) varied $P_{N,0}$ from 400 to 1200 to 6500 N, while keeping everything else constant. The results shown in Figs. 3(c)–3(e), respectively, demonstrate that increasing $P_{N,0}$ decreases both λ_{RB} and A_{RB}.

In a third set, we compared runs 60-0.13-400 and 160-0.05-400, shown in Figs. 3(b) and 3(f), respectively. Here, we varied t but kept $P_{N,0}$ at 400 N and the total deck thicknesses constant at $\approx$7.83 $\pm$ 0.17 mm. To accomplish the latter, we had to start with more spd for the thinner sheets. Lastly, we compared 30-0.13-6500 and 70-0.05-6500. In this case, $P_{N,0}$ at 6500 N and the total deck thickness was held at 3.87 $\pm$ 0.01 mm, and t was varied. Comparing the vertically stacked Figs. 3(b) and 3(f) or 3(e) and 3(g), it is clear that decreasing t resulted in decreases in both λ_{RB} and A_{RB}.

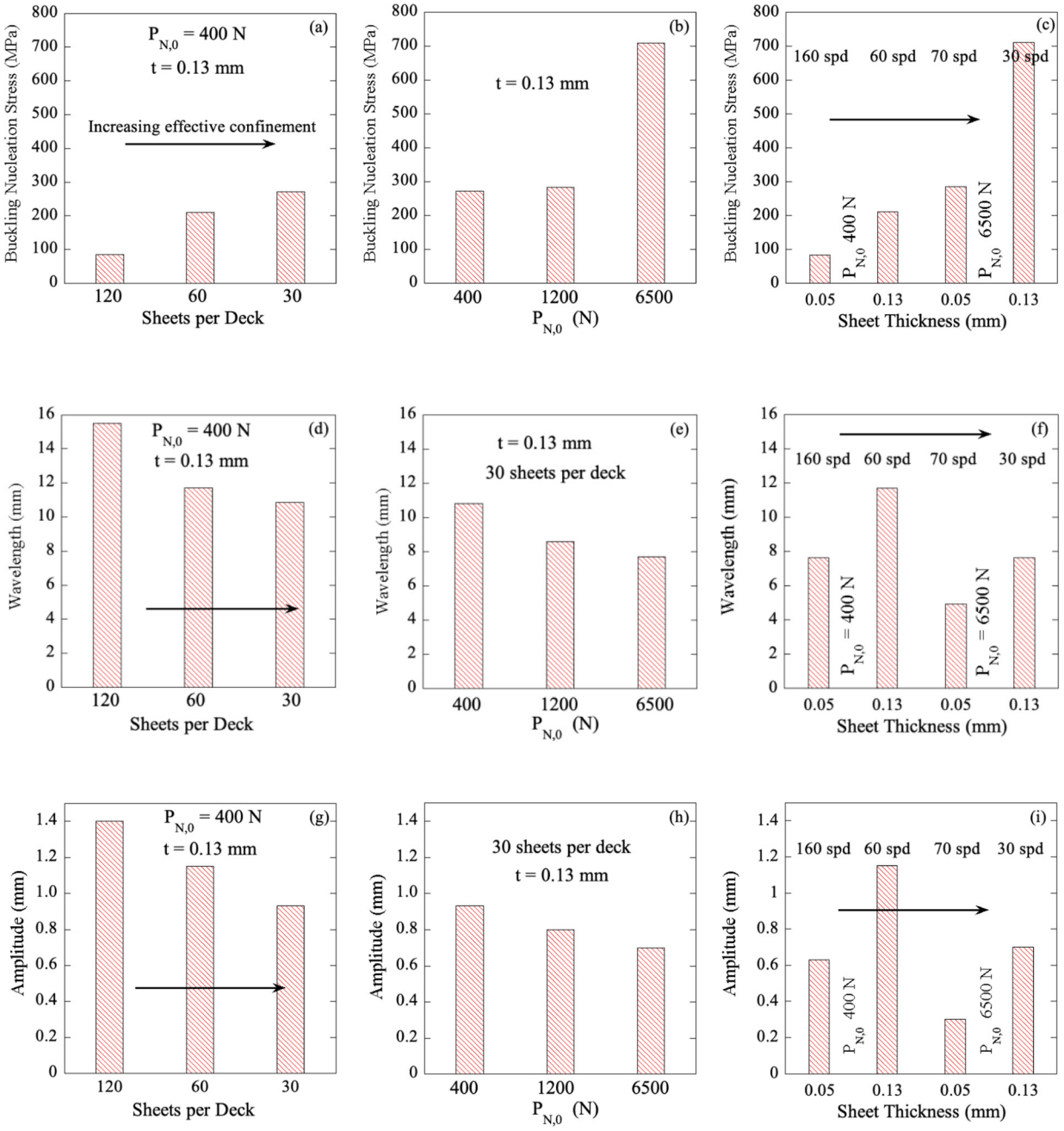

FIG. 5. (a) σ_{Bu} as a function of decreasing number of sheets 120, 60, and 30 at $P_{N,0}$ of 400 N. (b) Same as (a) but with $P_{N,0}$ of 400, 1200, and 6500 N for the same total number of sheets (30). (c) σ_{Bu} as a function of t and $P_{N,0}$ of 400 N (two left columns) and 6500 N (two right columns), while keeping total thickness of decks constant. (d) λ_{RB} for same variables as (a). (e) λ_{RB} for same variables as (b). (f) λ_{RB} for same variables as (c). (g) A_{RB} for same variables as (a). (h) A_{RB} for same variables as (b). (i) A_{RB} for same variables as (c). Horizontal arrows denote direction of increasing effective and/or direct constraining pressure.

Figure 4 plots, on the same scale, the indentation stress-strain curves obtained as a function of the variables listed above. Like in our previous work [11], the stress-strain curves are composed of three regimes: an initial generally linear regime, a second region where the stress appears to plateau or level off, and lastly, a set of nearly fully recoverable nested loops. The point at which the behavior changes from linear to nonlinear elastic manner is defined as the point of buckling nucleation stress σ_{Bu}. At that stress, a buckling instability occurred, and collective, oppositely signed RBs were nucleated below the perturbation source and rapidly spanned in a wavelike manner away from the indenter. That can be clearly noticed in the cases where $P_{N,0}$ was 6500 N [e.g., Figs. 4(b) and 4(d)], where a clear and distinct drop in stress is observed at the end of the linear regime.

The experimentally determined σ_{Bu} values obtained as a function of the aforementioned variables are summarized in Fig. 5. Note that, in all plots, moving to the right corresponds to higher confining stresses, effective and/or direct. The results are also summarized in

TABLE I. Comparison of theoretical and experimental results. In first column, first number refers to the number of layers per deck, the second t in mm, and the third $P_{N,0}$. Last column lists η. The percent difference is the experimental minus the theoretical by the experimental value. Number of layers deformed by the indenter are shown in brackets in first column.

Continuum scale results										
	Theory			Experiment			Difference (%)			η
Test conditions	2L (mm)	P_{crit} (N)	Mode	λ (mm)	P_{BK} (N)	Mode	λ (mm)	P_{crit} (N)	Mode	
120-0.13-400 (19)	15.6	6632	5.1	15.5	6190	5	−1%	−7%	−3%	120
60-0.13-400 (12)	11.9	7309	6.7	11.7	9497	6	−2%	23%	−12%	239
30-0.13-400 (10)	10.8	7277	7.4	10.8	10 241	8	0%	29%	7%	265
30-0.13-1200 (10)	10.7	7354	7.5	8.6	9975	9	−24%	26%	16%	112
30-0.13-6500 (11)	11.1	7649	7.2	7.7	17 470	11	−43%	56%	34%	62
70-0.05-6500 (35)	6.5	4459	12.3	4.9	12 197	16	−33%	63%	23%	20
160-0.05-400 (23)	7.1	2499	11.3	7.6	3138	10	7%	20%	−13%	168
Atomistic scale results										
	Theory			MD simulation			Difference (%)			
Initial confining pressure (bar)	2L (nm)	P_{crit} (nN)	Mode	λ (nm)	P_{BK} (nN)	Mode	λ (nm)	P_{crit} (nN)	Mode	η
0	10.4	16.9	9.6	4.5	15	19	−133%	−13%	49%	12
1000	10.5	18.5	9.6	4.3	15.5	20	−143%	−20%	52%	8
5000	10.5	21.9	9.5	4.2	17.5	21	−150%	−25%	55%	3

Table I. From the findings, the following observations become apparent:

(i) Increasing the effective confining stresses on the decks increases σ_{Bu} [Figs. 5(a) and 5(b)] and the number of modes (Table I) but decreases both λ_{RB} and A_{RB} [Figs. 5(d), 5(e), 5(g), and 5(h)].

(ii) For the same deck thickness and $P_{N,0}$, decreasing t decreases σ_{Bu} [Fig. 5(c)], λ_{RB} [Fig. 5(f)], and A_{RB} [Fig. 5(i)].

(iii) For the same deck thickness and $P_{N,0}$, decreasing t changes the shape of the stress-strain envelope from lenticular to almost rectangular, especially at high $P_{N,0}$ [Fig. 4(d)].

(iv) At the highest $P_{N,0}$ of 6500 N, nucleation of buckling boundaries results in a clear drop in indentation stress [Figs. 4(b) and 4(d)]. Not surprisingly, this drop correlates exactly with the onset of buckling in the images.

V. DISCUSSION

From the totality of our results, confinement plays a key role in the buckling wavelengths and nucleation stresses. The other key factor that is fully consistent with buckling theory is that the individual thickness of the layers also highly influences the results.

A. Buckling loads and wavelengths

Table I compares the theoretically and experimentally determined values of buckling loads, wavelengths, and modes. Figures 6(a) and 6(b) plot the same information together with those of Edmunds *et al.* [3] on thin paper sheets confined by foam as well as calculated vs observed values based on graphite indentations performed at the nanoscale from MD simulations [11]. To model verification at the atomistic scale, Eqs. (4) and (5) were used to calculate the critical load and wavelength values for graphite. The elastic modulus of graphite was obtained from the slope of the initial linear portion of force after conversion to stress-strain curves (Fig. 5(c) in [11]) to be 800 GPa. The number of buckled layers n was an input to the model and was visually counted at $h_{max} = 2.5$ nm from the simulation images. For the calculation of the moment of inertia, Eq. (1), the width $b = 1$ nm and t were taken to be equal to the thickness of an individual graphene layer or 0.335 nm. The spring constant k was calculated, as explained by Eq. (2), from the slope of confinement pressure vs indentation depth (see Fig. 4(f) in [11]) which is a direct output of the MD code. The values of wavelength, amplitude, and number of buckled layers of MD simulated graphite were measured from still frames using IMAGEJ.

Based on the continuum results with the experiments conducted in this paper, when $P_{N,0}$ is 400 N, or at low levels of confinement, the agreement between theory and experiment is good (i.e., for $\eta > 112$, all but one prediction of the critical load, amplitude, and buckling mode are within 23% of the experimental findings). Interestingly, the model predictions are relatively insensitive to t or the total number of layers in the deck (listed in the first three and last entries in Table I). This is especially true since, experimentally, our method of calculating stress is less than ideal.

At higher $P_{N,0}$ values, the agreement is less satisfactory. One of the main reasons for the discrepancy is the breakdown in the assumption than $\eta \gg 1$ (last column in Table I). From the results shown in Table I and Fig. 6, it appears that our model is less predictive when $\eta \leqslant 112$. We purposely plot the high confinement results to show where the current theory breaks down. Future work will explore either a correction for higher confinement or a full nonlinear solution to remove the limiting geometric assumption of the curvature embedded in the model. These comments notwithstanding, the agreement between theory and experiment in our case and that of Edmunds *et al.* [3] is significant, especially given the very differing materials tested (steel vs paper) and radically different levels of support (quite stiff steel support vs foam).

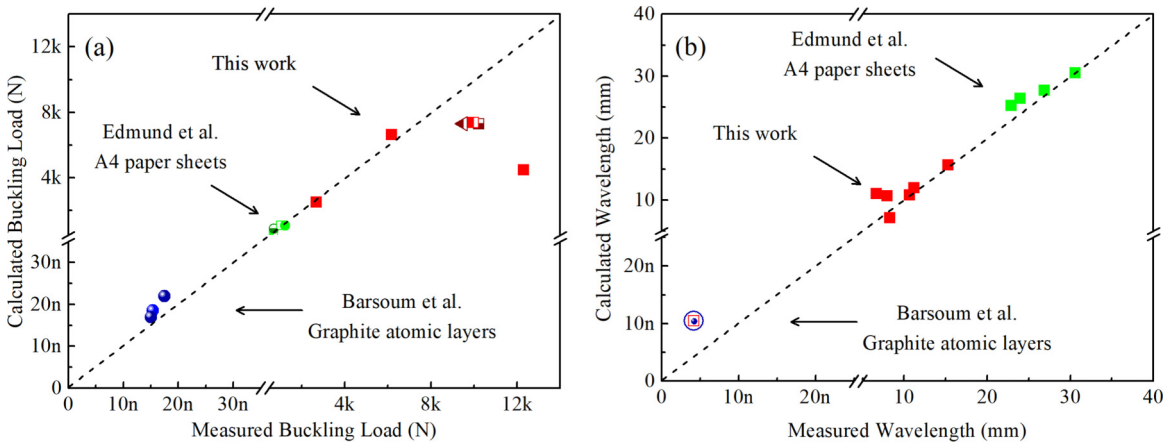

FIG. 6. Comparison of measured and calculated values of (a) buckling load and (b) λ_{BR} at the continuum and atomistic scales. The results of the paper of Edmund *et al.* [3] with a soft foam foundation are also plotted in green. The corresponding values for graphite ripplocations derived from DFT calculations at the atomistic scale are plotted as blue spheres/circles [11]. Here, *n* stands for nano. Note this is not a log-log plot.

By looking at the atomistic scale results, the agreement of the analytical model with MD ripplocation results suggests the model applies to atomic layers as well. Noteworthily, like the continuum tests, the agreement between theory and MD results is best at large η values, at which no/low confining pressure was applied, and becomes increasingly less good when $P_{N,0}$ is 5000 bar (last row in Table I). Notably, the model is robust in that it can predict the buckling nucleation stress with a maximum difference of 25% relative to the simulation outputs. However, due to the complex and differing mechanics at the nanoscale, the continuum theory poorly predicts the wavelength at which these instabilities occur and is a topic of future study.

B. Energy dissipated per cycle

All the nested loops shown in Fig. 4 are fully recoverable. Figure 7(a) plots W_d as a function of ε_{RB} for the variables tested here. Under these conditions and further assuming $\sigma_{RB} \approx 2\tau_{RB}$, the following relationship is approximately valid:

$$W_d = 2\tau_{RB}\gamma_{RB} \approx (1+\nu)\sigma_{RB}\varepsilon_{RB}, \tag{7}$$

where γ_{RB}, ε_{RB}, and ν are the applied shear, normal strains, and Poisson's ratio, respectively. Also, τ_{RB} and σ_{RB} are the shear and normal stresses needed to move the RBs. Here, τ_{RB} can be considered a critical resolved shear stress for RBs. The factor of 2 accounts for energy dissipated during loading and unloading. If we further assume Coulombic friction, viz. $P_S = \mu P_N$, where P_N and P_S are the average loads acting normal and parallel to the layers during a cycle, respectively, then combining the fact that $\sigma_{RB} = P_S/A_{ind}$—where A_{ind} is the indented area—together with Eq. (7), it follows that

$$W_d \approx (1+\nu)\mu\frac{P_N\varepsilon_{RB}}{A_{ind}}. \tag{8}$$

If this equation is valid, and μ is not a function of P_N, then plots of W_d vs $(P_N \times \varepsilon_{RB})/A_{ind}$ should yield straight lines with

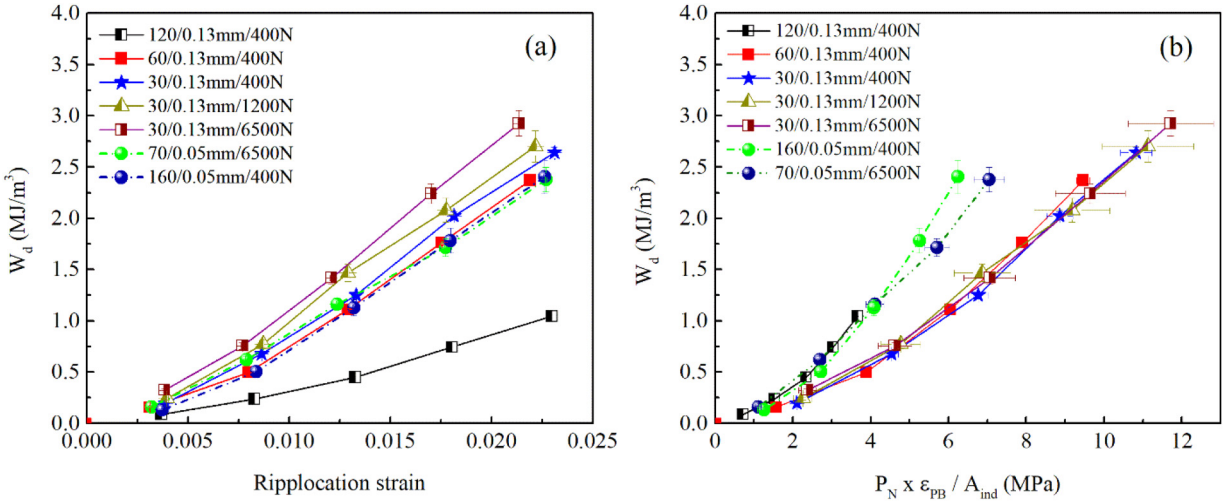

FIG. 7. (a) W_d vs ε_{RB} for various variables shown on panels, and (b) W_d vs $(P_N \times \varepsilon_{BR})/A_{ind}$ for all nested loops shown in Fig. 4. Slopes of lines $\approx \mu(1+\nu)$. The two lines with higher slopes (circles) were obtained on decks with thinner sheets.

TABLE II. Least squares of slopes of lines shown in Fig. 7(b). The μ values are calculated assuming $\nu = 0.3$.

	120/1.3/400	60/1.3/400	30/1.3/400	30/1.3/1200	30/1.3/6500	70/0.05/6500	160/0.05/400
Slope	0.28 ± 0.03[a]	0.28 ± 0.03	0.28 ± 0.05	0.28 ± 0.11	0.28 ± 0.10	0.33 ± 0.08[a]	0.35 ± 0.07[a]
μ	0.21 ± 0.03	0.22 ± 0.03	0.22 ± 0.05	0.21 ± 0.11	0.22 ± 0.10	0.26 ± 0.08	0.27 ± 0.07

[a]Only first three points in Fig. 7(b) were used to calculate these values since, beyond these points, the curves are quite nonlinear, when all our assumptions are for a linear system.

slopes equal to $\mu(1 + \nu)$. Figure 7(b) shows that to indeed be the case. Least squares fit of the lines yield the slopes listed in the second row of Table II. If one assumes ν to be 0.3, then the μ values listed in the last row in Table II are obtained.

Given the simplicity of the model used to derive Eq. (8), the results shown in Fig. 7(b) are quite gratifying for several reasons:

(i) The fact that the μ values listed in the last row in Table II, averaging 0.23 ± 0.03, are in excellent agreement with the experimentally measured μ values of 0.23 and 0.27 for the thick and thin sheets, respectively, is remarkable and lends credence to our experiments, analysis and relatively simple model.

(ii) The fact that the quite different—in terms of the absolute stress levels, shapes, confining loads, etc.—recoverable hysteretic loops shown in Fig. 4 collapse onto a universal curve [compare Fig. 7(a) to 7(b)] suggests our simple model captures the physics of W_d surprisingly well indeed. This in turn implies that Coulombic friction, viz. $P_S = \mu \mathrm{P_N}$, is applicable and that μ is not a strong function of P_N.

(iii) The slight curvature seen in the curves, however, suggest that μ may not be totally independent of P_N. Strictly speaking, one should therefore only take the initial slopes of the lines plotted in Fig. 7(b). However, doing so may slightly change the values listed in Table II but not shed more light on the problem and was eschewed—except in the two cases where $t = 0.05$ mm, where the curvature was more pronounced—to avoid any subjectivity in determining how many points to include in calculating the initial slopes.

These results suggest that a straightforward method to increase W_d is to start with thinner sheets.

C. Plastic deformation vs energy dissipated per cycle

In all experiments conducted herein, after the nested loops were obtained, the indenter was totally retracted and then indented into the deck one last time to obtain a second full cycle [denoted by the area colored yellow in Fig. 1(b)] before its ultimate retraction, which accounts for the two largest loops observed in Fig. 4. In all cases, the area of the second full or last cycle is a fraction of the first. The difference between areas of cycles 1 and 2—given by the area colored yellow in Fig. 1(b)—represents the energy dissipated in the first cycle in plastically deforming the sheets labeled W_{pl} in Fig. 8. From the totality of the results plotted in Fig. 8, the following observations can be made:

(i) W_{pl} increased with $P_{N,0}$ (horizontal arrows), whether actual or effective [Figs. 8(a) and 8(b)].

(ii) Another important factor is t. Under comparable conditions, W_{pl} values for the thicker sheets are ~3 times those of the thinner ones [Figs. 8(c) and 8(d)]. Thick sheets that are highly confined are more heavily deformed in the first cycle than loosely confined thinner ones. Said otherwise, for the same $P_{N,0}$ and deck thicknesses, W_{pl}/W_d increases as t increases. It follows that, to minimize the W_{pl}/W_d ratio, thin sheets that are not too highly constrained should be used.

Lastly, images of postcycling thin and thick sheets, indented with a $P_{N,0}$ of 6500 N, are shown in Fig. 9(a), from which it is clear the thin sheets (top) are less deformed than their thicker (bottom) counterparts. The corresponding W_{pl}/W_d ratios for these thick and thin sheets were 1.6 and 0.8. One of the consequences of this plastic deformation is a large decrease in σ_{crit} upon reloading. Once the sheets have been deformed the first time, the nucleation of subsequent RBs occurs at significantly lower stresses (Fig. 4).

Unlike the thin steel sheets, the thick sheets buckled locally, forming a KB near the indenter [see red circle in Fig. 9(c)]. Before converting to a KB, the same location sustained a RB. The same behavior was observed when thin Al sheets were loaded by the same indenter used in this paper. At shallow depths, the response was fully reversible and like the response described in this paper. When the indenter was thrust deeper into the layers, RBs close to the indenter converted to KBs that were no longer reversible [11]. In other words, these results demonstrate that RBs appear to be KB precursors in the continuum sense.

D. Initial slopes of stress-strain curves

In our NI work on various layered and nonlayered solids, the initial slopes of the NI stress vs strain were in most cases equal to the operative elastic constants [18,49–52]. The situation here is fundamentally different since the initial slopes in Fig. 4 are orders of magnitude lower than Young's moduli of our spring steel ($E \sim 200$ GPa). What occurs here instead is an almost immediate bending of the sheets [Fig. 9(b)] up to the point when the RBs nucleate. Vestiges of this bending can be clearly seen in the postindented thin [Fig. 9(c)] and thick [Fig. 9(d)] sheets. This bending was verified from careful examination of images in the linear regime. It is important to note this is not a buckling but bending mode.

Lastly, before concluding, we note that there is a significant amount of work on buckling mechanics in the literature. The following points, however, differentiate this paper from previous work and are thus crucial considerations: (i) In the mechanics literature, the main emphasis is on predicting the buckling stresses; here, buckling is just the start of the phenomenon of interest. (ii) We are more interested in the KNE regime, where nearly reversible/recoverable RBs are operative. As far as we are aware, the buckling community rarely

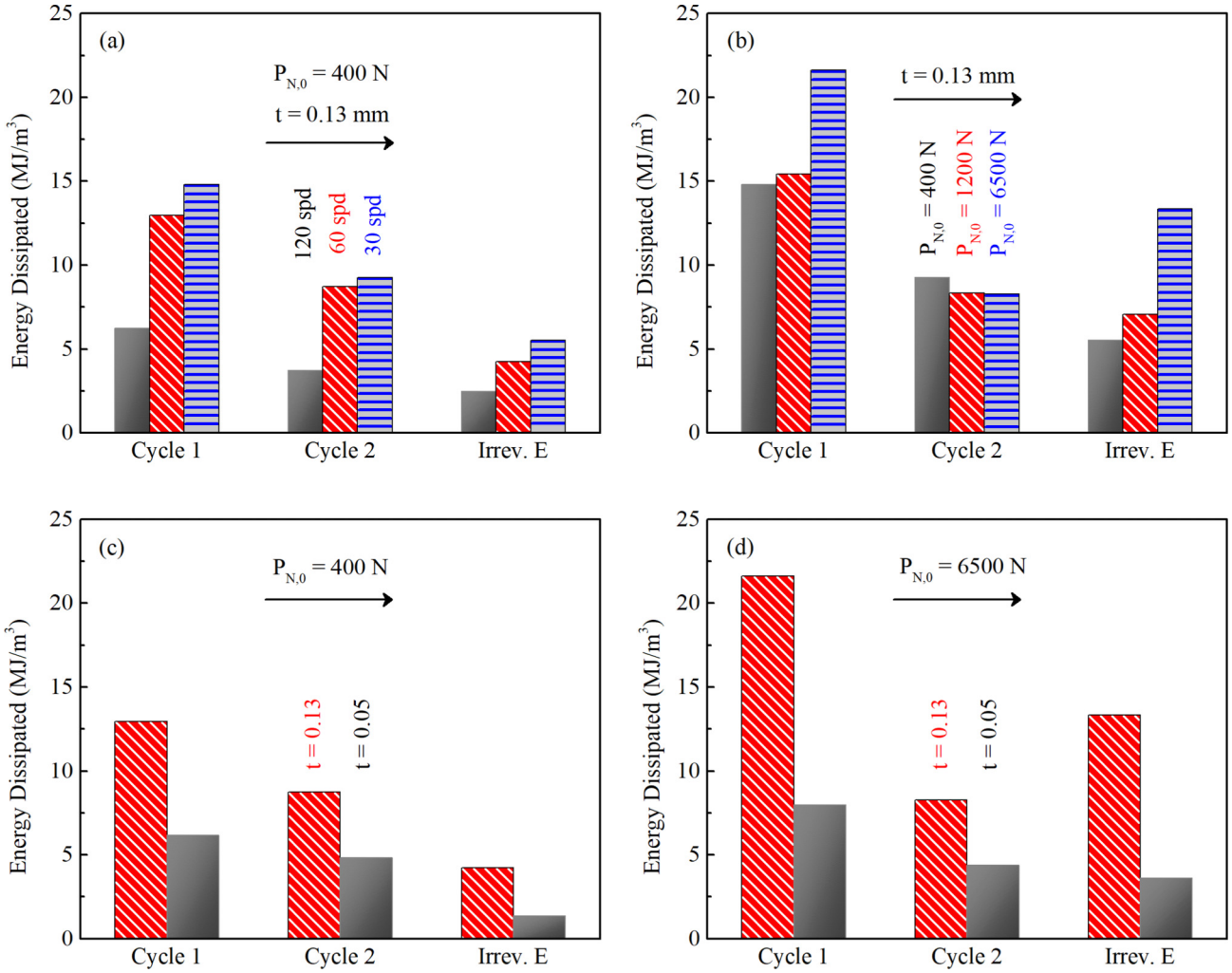

FIG. 8. Comparison of energies dissipated during cycles 1 and 2 and the difference W_{pl}, which is a measure of plastic deformation during cycle 1 as a function of (a) sheets per deck (spd), (b) $P_{N,0}$, (c) sheet thickness at $P_{N,0} = 400$ N, and (d) same as (c) but for $P_{N,0} = 6500$ N. Horizontal arrows denote direction of increasing effective and/or direct constraining pressure.

addressed the reversible stress-strain curves, either on the macroscale or under various nanoindenters. (iii) Herein, we show that W_d can be simply modeled by Coulombic friction between the sliding sheets.

We also show a strong correlation between the predicted and actual buckling load and number of buckle modes at multiple length scales (across material systems). Ultimately, we hope to understand buckling and energy dissipation phenomena which may share commonalities with atomic buckling in layered solids.

VI. CONCLUSIONS

In graphite and other layered solids, the application of compressive loads can result in the formation of RBs. Little is currently known about the mechanics of RBs or why they are essentially fully recoverable and dissipative. To explore this energy dissipation at the continuum scale, we studied laterally confined thin steel sheets, indenting them with a cylindrical indenter as a function of effective confining pressure and the thicknesses of individual sheets. We found that increasing the confining pressure, thicknesses of individual sheets, and/or reducing the number of layers or spd increased the load at which ripplocations nucleate. Concomitantly, the wavelengths and amplitudes of the ripples decreased.

We applied a confined buckling folding mechanics model that considered frictional, bending, and foundation energies to predict the nucleation stresses and associated wavelengths of the steel layers. The predictions agreed with our experimental results, especially at low confining pressures, and were surprisingly good at predicting nucleation loads even down to the atomistic level with graphite ripplocation MD results. Interestingly, μ between the steel sheets did not affect these parameters. Where μ played a crucial role in these experiments, however, was in accounting for the energy dissipated per unit volume per cycle. By assuming Coulombic friction, we recovered the experimentally measured values of μ.

Lastly, and while there is still much to be learned, the results of our experiments place the mechanics of ripplocation

(a)

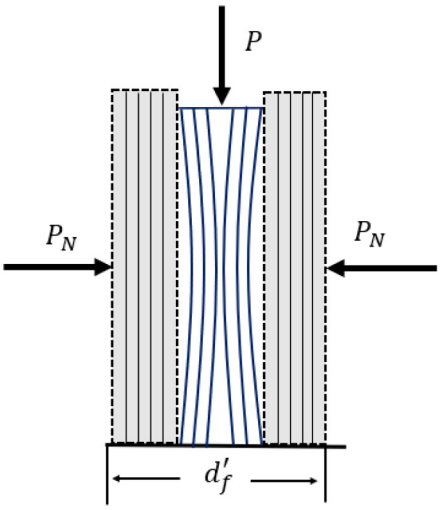

(b) (c) (d)

FIG. 9. (a) Picture of postcycling thin (top) and thick (bottom) sheets indented for $P_{N,0} = 6500$ N. (b) Schematic of buckling mode responsible for linear regime in Fig. 4. (c) Same as (a) but showing full deck for $t = 0.13$ mm, and (d) same as (c) but for $t = 0.05$ mm.

nucleation, propagation, and energy dissipation at the atomic scale in a degree of correlation with the results from buckling of continuum layered systems. The work to discover the extent of the commonalities, mechanism differences, and potential universality of the buckle/ripple phenomenon across length scales is currently ongoing.

ACKNOWLEDGMENTS

This paper was funded by the Civil, Mechanical and Manufacturing Innovation Division of the National Science Foundation (NSF; Grant No. 1728041). L.L. recognizes NSF CAREER Grant No. 1939838.

[1] M. A. Wadee, G. W. Hunt, and M. A. Peletier, Kink band instability in layered structures, J. Mech. Phys. Solids **52**, 1071 (2004).

[2] M. A. Wadee and R. Edmunds, Kink band propagation in layered structures, J. Mech. Phys. Solids **53**, 2017 (2005).

[3] R. Edmunds, G. W. Hunt, and M. A. Wadee, Parallel folding in multilayered structures, J. Mech. Phys. Solids **54**, 384 (2006).

[4] G. Hunt, R. Butler, and C. Budd, Geometry and mechanics of layered structures and materials (theme issue), Phil. Trans. R. Soc. A **370**, 1723 (2012).

[5] P. J. Hudleston and S. H. Treagus, Information from folds: a review, J. Struct. Geol. **32**, 2042 (2010).

[6] A. M. Johnson, *Styles of Folding: Mechanics And Mechanisms of Folding of Natural Elastic Materials* (Elsevier, Amsterdam, 1977), Vol. 11.

[7] M. A. Biot, Folding instability of a layered viscoelastic medium under compression, Proc. R. Soc. Lond. A **242**, 444 (1957).

[8] B. Budiansky, N. A. Fleck, and J. C. Amazigo, On kink-band propagation in fiber composites, J. Mech. Phys. Solids **46**, 1637 (1999).

[9] S. Kyriakides and A. E. Ruff, Aspects of the failure and post-failure of fiber composites in compression, J. Compos. Mater **31**, 1633 (1997).

[10] S. Narayanan and L. S. Schadler, Mechanisms of kink-band formation in graphite/epoxy composites: A micromechanical experimental study, Compos. Sci. Technol. **59**, 2201 (1999).

[11] M. W. Barsoum, X. Zhao, S. Shanazarov, A. Romanchuk, S. Koumlis, S. J. Pagano, L. Lamberson, and G. Tucker, Ripplocations: a universal deformation mechanism in layered solids, Phys. Rev. Mater. **3**, 013602 (2019).

[12] M. W. Barsoum, A. Murugaiah, S. R. Kalidindi, and Y. Gogotsi, Kink bands, nonlinear elasticity and nanoindentations in graphite, Carbon **42**, 1435 (2004).

[13] M. W. Barsoum and G. Tucker, Deformation of layered solids: ripplocations not basal dislocations, Scrip. Mater. **139**, 166 (2017).

[14] D. Frieberg, M. W. Barsoum, and G. Tucker, Nucleation of ripplocations through atomistic modeling of surface nanoindentation in graphite, Phys. Rev. Mater. **2**, 053602 (2018).

[15] J. Griggs, A. Lang, J. Gruber, G. Tucker, M. Taheri, and M. W. Barsoum, Spherical nanoindentation and transmission electron microscopy evidence for ripplocations in Ti_3SiC_2, Acta Mater. **131**, 141 (2017).

[16] J. Gruber, A. Lang, J. Griggs, M. Taheri, G. Tucker, and M. W. Barsoum, Evidence for bulk ripplocations in layered solids, Sci. Rep. **6**, 33451 (2016).

[17] J. Aslin, E. Mariani, K. Dawson, and M. W. Barsoum, Ripplocations provide a new mechanism for the deformation of phyllosilicates in the lithosphere, Nat. Commun. **10**, 686 (2019).

[18] H. O. Badr, A. Champagne, T. Ouisse, J.-C. Charlier, and M. W. Barsoum, Elastic properties and hardness values of V_2AlC and Cr_2AlC single crystals, Phys. Rev. Mater. **4**, 083605 (2020).

[19] S. Basu and M. W. Barsoum, On spherical nanoindentations, kinking nonlinear elasticity of mica single crystals and their geological implications, J. Struct. Geology **31**, 791 (2009).

[20] A. Kushima, X. Qian, P. Zhao, S. Zhang, and J. Li, Ripplocations in van der Waals layers, Nano Lett. **15**, 1302 (2015).

[21] B. März, K. Jolley, R. Smith, and H. Wu, Near-surface structure and residual stress in as-machined synthetic graphite, Mater. Des. **159**, 103 (2018).

[22] B. März, K. Jolley, T. J. Marrow, Z. Zhou, M. Heggie, R. Smith, and H. Wu, Mesoscopic structure features in synthetic graphite, Mater. Des. **142**, 268 (2018).

[23] A. V. Alaferdov, R. Savu, M. A. Canesqui, Y. V. Kopelevich, R. R. da Silva, N. N. Rozhkova, D. A. Pavlov, Yu. V. Usov, G. M. de Trindade, and S. A. Moshkalev, Ripplocation in graphite nanoplatelets during sonication assisted liquid phase exfoliation, Carbon **129**, 826 (2018).

[24] J. G. Ramsey, *Folding and Fracturing of Rocks* (McGraw-Hill, New York, 1967).

[25] B. E. Hobbs, W. D. Means, and P. F. Williams, *An Outline of Structural Geology* (John Wiley & Sons, New York, 1976).

[26] N. J. Price and J. W. Cosgrove, *Analysis of Geological Structures* (Cambridge University Press, Cambridge, 1990).

[27] J. B. Currie, H. W. Patnode, and R. P. Trump, Development of folds in sedimentary strata, Bull. Geol. Soc. Am. **73**, 655 (1962).

[28] A. M. Johnson and E. Honea, A theory of concentric, kink and sinusoidal folding and of monoclinal flexuring of compressible, elastic multilayers. III. Transition from sinusoidal to concentric-like to chevron folds, Tectonophysics **27**, 1 (1975).

[29] P. H. Kuenen and L. U. de Sitter, Experimental investigation into the mechanism of folding, Leidsche Geol. Med. **XII**, 219 (1938).

[30] P. Blay, J. W. Cosgrove, and J. M. Summers, An experimental investigation of the development of structures in multilayers under the influence of gravity, J. Geol. Soc. Lond **133**, 329 (1977).

[31] C. J. Budd, R. Edmunds, and G. W. Hunt, Nonlinear model for parallel folding with friction, Proc. R. Soc. London Ser., A **459**, 2097 (2003).

[32] M. A. Wadee, Experimental evaluation of interactive buckle localization in compression sandwich panels, J. Sandw. Struct. Mater **1**, 230 (1999).

[33] H. Chai, The post-buckling response of a bi-laterally constrained column, J. Mech. Phys. Solids **46**, 1155 (1998).

[34] S. Katz and S. Givli, The post-buckling behavior of a beam constrained by springy walls, J. Mech. Phys. Solids **78**, 443 (2015).

[35] B. Roman and A. Pocheau, Postbuckling of bilaterally constrained rectangular thin plates, J. Mech. Phys. Solids **50**, 2379 (2002).

[36] T. Su, J. Liu, D. Terwagne, P. M. Reis, and K. Bertoldi, Buckling of an elastic rod embedded on an elastomeric matrix: planar vs. non-planar configurations, J. Soft Matter **10**, 6294 (2014).

[37] P. Celli, C. McMahan, B. Ramirez, A. Bauhofer, C. Naify, D. Hofmann, B. Audoly, and C. Daraio, Shape-morphing architected sheets with non-periodic cut patterns, J. Soft Matter **14**, 9744 (2018).

[38] B. Budiansky and N. A. Fleck, Compressive kinking of fiber composites: A topical review, Appl. Mech. Rev. **47**, S246 (1994).

[39] C. R. Schultheisz and A. M. Waas, Compressive failure of composites, part I: Testing and micromechanical theories, Prog. Aerosp. Sci. **32**, 1 (1996).

[40] A. M. Waas and C. R. Schultheisz, Compressive failure of composites, part II: experimental studies, Prog. Aerosp. Sci. **32**, 43 (1996).

[41] N. A. Fleck, S. Sivashanker, and M. P. F. Sutcliffe, Compressive failure of composites due to microbuckle growth, Eur. J. Mech. A/Solids **16**, 65 (1997).

[42] N. A. Fleck and J. Y. Shu, Microbuckle initiation in fibre composites: a finite element study, J. Mech. Phys. Solids **43**, 1887 (1995).

[43] S. Kyriakides, S. Arseculeratne, E. J. Perry, and K. M. Liechti, On the compressive failure of fiber reinforced composites, Int. J. Solids Struct. **32**, 689 (1995).

[44] M. P. F. Sutcliffe and N. A. Fleck, Microbuckle propagation in fibre composites, Acta Metall. **45**, 921 (1997).

[45] T. Takahashi, M. Ueda, K. Iizuka, A. Yoshimura, and T. Yokozeki, Simulation on kink-band formation during axial compression of a unidirectional carbon fiber-reinforced plastic constructed by x-ray computed tomography images, Adv. Compos. Mater. **28**, 347 (2019).

[46] A. B. Jensen, J. Thesbjerg, J. L. Wind, and H. M. Jensen, Kink band predictions in fiber composites using periodic boundary conditions, Compos. Struct. **207**, 331 (2019).

[47] See Supplemental Material at http://link.aps.org/supplemental/10.1103/PhysRevMaterials.5.093603 for the changes/development of the ripplocation boundaries' wavelength as a function of the indentation depth.

[48] C. A. Schneider, W. S. Rasband, and K. W. Eliceiri, NIH Image to ImageJ: 25 years of image analysis, Nat Methods **9**, 671 (2012).

[49] S. Basu, M. W. Barsoum, and S. R. Kalidindi, Sapphire: a kinking nonlinear elastic Solid, J. Appl. Phys. **99**, 063501 (2006).

[50] S. Basu, A. Moseson, and M. W. Barsoum, On the determination of indentation stress-strain curves using spherical indenters, J. Mater. Res. **21**, 2628 (2006).

[51] S. Basu and M. W. Barsoum, Deformation micromechanisms of ZnO single crystals as determined from spherical nanoindentation stress-strain curves, J. Mater. Res. **22**, 2470 (2007).

[52] B. Anasori, K. E. Sickafus, I. O. Usov, and M. W. Barsoum, Spherical nanoindentation study of effect of ion irradiation on deformation micromechanism of $LiTaO_3$ single crystals, J. Appl. Phys. **110**, 023516 (2011).